Exploring the math xmlns="http://www.w3.org/1998/Math/MathML">mrow>mi>A/mi>/mrow>/math>-V-Sb landscape beyond math xmlns="http://www.w3.org/1998/Math/MathML">mrow>mi>A/mi>msub>mi mathvariant="normal">V/mi> mn>3/mn>/msub>msub>mi>Sb/mi>mn>5/mn>/msub>/ mrow>/math>: A case study on the math xmlns="http://www.w3.org/1998/Math/MathML">mrow>mi mathvariant="normal">K/mi>msub>mi mathvariant="normal">V/mi>mn>6/mn>/msub>msub>mi>Sb/mi>mn>6/mn>/msub>/mrow>/math> Kagome compound

Aishwarya Mantravadi, Volodymyr Gvozdetskyi, Arka Sarkar, Yaroslav Mudryk, and Julia V. Zaikina

Phys. Rev. Materials **7**, 115002 — Published 15 November 2023

DOI: 10.1103/PhysRevMaterials.7.115002

Exploring the *A*-V-Sb landscape beyond AV_3Sb_5: a case study on KV_6Sb_6 Kagome compound

Aishwarya Mantravadi,[1] Volodymyr Gvozdetskyi,[1#] Arka Sarkar,[1,2] Yaroslav Mudryk,[2] Julia V. Zaikina[1]

[1] *Department of Chemistry, Iowa State University, Ames, Iowa 50011, United States*

[2] *Ames National Laboratory of US DOE, Iowa State University, Ames, Iowa 50011, United States*

[#] Present Address: Department of Chemistry, University of Alberta, Edmonton, Alberta, Canada T6G 2G2

Abstract. Kagome compounds have garnered attention in the past few years for their intriguing magnetic properties arising from spin frustration dictated by the geometry of the Kagome sublattice. In this report, we highlight the success of the unconventional hydride route for the fast and easy synthesis of the new Kagome compound KV_6Sb_6. High-temperature *in-situ* powder X-ray diffraction studies proved to be useful in hinting at the existence of KV_6Sb_6, identifying its synthesis conditions, and understanding the reaction mechanism. The crystal structure for KV_6Sb_6 was determined from high-resolution powder X-ray diffraction data. The compound has a layered structure ($R\overline{3}m$, a = 5.5318(9) Å, c = 34.23(3) Å, V = 907.0(8) Å^3, Z = 3 at room temperature) and features a Kagome bilayer of V atoms. KV_6Sb_6 is isostructural to the previously reported RbV_6Sb_6 and CsV_6Sb_6 compounds. KV_6Sb_6 is thermally stable in vacuum up to 1173 K, as evident from the high-temperature *in-situ* powder X-ray diffraction and differential scanning calorimetric analysis. Investigation of magnetic properties for KV_6Sb_6 between 2–300 K reveals temperature-independent paramagnetism and an absence of superconductivity, similar to the Rb and Cs analogs. Furthermore, we compare the magnetic properties of KV_3Sb_5, another ternary Kagome compound, synthesized via two different methods: a new hydride route and the traditional route from elements. Low-temperature transport property measurements of KV_6Sb_6 indicate metallic behavior and an intrinsically low thermal conductivity of 1.0 $W\cdot K^{-1}m^{-1}$ at 300 K. The layered structure of KV_6Sb_6 makes it an attractive candidate for deintercalation and doping studies to tune both magnetic and transport properties, laying a foundation for further studies.

Keywords: antimonide, Kagome compound, layered material, hydride synthesis, *in-situ* XRD, thermoelectric, low thermal conductivity.

Introduction.

Investigation of the structure-property relationships in inorganic solids is crucial for pinpointing the unique structural features that can yield interesting magnetic properties. Several materials classes have been extensively studied in the pursuit of discovering and realizing intriguing magnetic behavior; one such example is the Kagome class of compounds. A Kagome lattice has a star-like geometric pattern comprising regular hexagons and triangles.[1,2] Structures of most of the Kagome compounds belong to the $R\overline{3}m$, $P6/mmm$, or $P6_3/mmc$ space groups, a consequence of the geometry of the Kagome sublattice.[2,3] This geometry inhibits perfect antiferromagnetic alignment of spins at the Kagome sites, causing magnetic frustration. Magnetic frustration contributes to the origin of distinctive electronic and magnetic characteristics found in the Kagome materials, such as superconductivity, quantum spin liquids, charge density wave order, and Dirac fermions.[3–8] Research efforts, both experimental and computational, have been geared towards an in-depth study of the influence of the structural features and bonding on the band structure for accurate and accelerated prediction of Kagome candidates.[2,3]

The exotic magnetic characteristics rendered possible by the geometry of the Kagome lattice have triggered a quest for prototype Kagome materials capable of realizing interesting physical properties. This quest has led to realizing Kagome nets in jarosite,[1,2,9–14] pyrochlores,[1,2,15–23] herberthismithes,[3,24,25] intermetallic Kagome compounds such as HoAgGe,[26] PrPdAl,[27] $DyNi_5Ge_3$,[28] and, most recently, the new family of intermetallic compounds AV_3Sb_5 (A = K, Rb, Cs).[29] The AV_3Sb_5 compounds crystallize in $P6/mmm$ space group and have a layered structure consisting of a Kagome lattice of vanadium atoms. Extensive work has been conducted to understand these compounds' electronic and magnetic properties.[30–43] Shortly after their discovery, superconductivity was unearthed in these compounds: KV_3Sb_5, $T_C = 0.92$ K; RbV_3Sb_5, $T_C = 0.93$ K; CsV_3Sb_5, $T_C = 2.5$ K.[30–33] Studies have also revealed unconventional chiral charge density wave (CDW) order in this family of alkali metal-vanadium antimonides: KV_3Sb_5, $T_{CDW} = 78$ K; RbV_3Sb_5, $T_{CDW} = 103$ K; CsV_3Sb_5, $T_{CDW} = 94$ K.[34–38] Furthermore, the energy of the Fermi level (E_F) was adjusted via doping to tune the superconducting transition temperature.[39–43] Recently, the isostructural ATi_3Bi_5 (A = Rb, Cs) compounds were reported extending the family to the bismuthides.[44–49]

The attractive science of the magnetic and electronic states in AV_3Sb_5 compounds fueled the search for new compounds in the A-V-Sb systems. This resulted in the discovery of two new families of compounds, namely AV_8Sb_{12} (A = Rb, Cs) and AV_6Sb_6 (A = K, Rb, Cs).[50–53] The AV_8Sb_{12} and AV_6Sb_6 compounds also have a layered structure with a single Kagome layer of vanadium atoms in AV_8Sb_{12} and a Kagome bilayer of vanadium atoms in AV_6Sb_6. Although the AV_8Sb_{12} and AV_6Sb_6 compounds are not superconducting under ambient conditions, superconductivity can be realized in the AV_6Sb_6 compounds under pressure (A = K, Rb, Cs).[52] Detailed reports describing the flux crystal growth, crystal structures, and properties can be found for the Rb and Cs analogs for the AV_6Sb_6 compounds; however, experimental details for the K analog (KV_6Sb_6) are lacking.[50–53]

While the quest for new Kagome materials or any new material is exciting, material synthesis is often challenging owing to the poor kinetics and high diffusion barriers of solid-state reactions.[54–56] This holds particularly true for the A-T-Sb ternary systems with early transition metals (A = Li, Na, K, Cs, Rb; T = Ti, V, Cr) due to the extreme difference in the reactivity of A (m.p. 300–453 K), T (m.p. 1941–2183 K) and Sb (m.p. 903 K). In the A-T-Sb ternary systems (A = Li, Na, K, Cs, Rb; T = Ti, V, Cr), only 10 compounds are known, mostly with vanadium.[29,44–53] The traditional solid-state synthesis, also referred to as the 'heat and beat' method, requires high temperatures and long annealing times to facilitate diffusion. Unconventional precursors can aid in overcoming the limitations posed by traditional routes. One such synthetic method is the hydride route, in which the soft alkali metal is replaced with its salt-like reactive alkali metal hydride.[57–63] The use of hydride allows for precise compositional control and intimate mixing of precursors via ball milling. Switching the alkali metal for its hydride typically leads to faster reactions at lower temperatures than traditional solid-state synthetic routes. The hydride route also allows for synthesizing ternary phases composed of elements with significantly different reactivities[59,60] and enables access to metastable phases.[60] Therefore, the hydride route is ideal for rapid phase exploration.

Herein, we report the hydride route as a fast and easy alternative for the synthesis of the KV_6Sb_6 compound in the form of microcrystalline powder. We present a detailed study of KV_6Sb_6 synthesis, crystal structure, and low-temperature magnetic and transport properties. Our advanced synthesis approach, guided by *in-situ* studies and compositional prediction via machine learning algorithm,[64,65] proved to be a powerful tool for probing the K-V-Sb system in search of new compounds.

Experimental section.

Chemicals. Vanadium powder (V, Alfa Aesar, 99.5%) was used as received. Potassium hydride powder (KH, 30 wt% dispersion in mineral oil, Sigma-Aldrich) was washed several times with toluene and dried in vacuum before use. Antimony powder was obtained by ball milling Sb shots (Sb, Alfa Aesar, 99.9999%) using SPEX mixer/mill 8000M for 60 minutes in a ball mill container with tungsten carbide WC inserts and two WC balls. All starting materials and samples were handled in an argon-filled glovebox with $p(O_2) < 1$ ppm and $p(H_2O) < 1$ ppm.

Synthesis. Synthesis of polycrystalline samples was carried out using the hydride route. For synthesis of KV_3Sb_5 and KV_6Sb_6, powders of KH, V and Sb were weighed in the desired molar ratio (total mass = 0.3 g) and loaded into a polycarbonate grinding vial with a methacrylate grinding ball. For V_3Sb_2, V and Sb powders were used for synthesis. The grinding vial was sealed into two polyethylene bags under argon atmosphere and the mixture was ball milled using SPEX mixer/mill 8000M for 6 minutes. The ball-milled powders were transferred to a tantalum tube (ID: 8.2 mm, OD: 9.4 mm; approx. length: 45 mm), which was sealed using an arc welder under argon atmosphere and then put into a silica reactor. The reactor is equipped with a Swagelok safety check valve to avoid over-pressurizing from the hydrogen gas released during the reaction. The setup was evacuated down to $2.7–3.0 \times 10^{-5}$ Bar pressure and placed into a programmable high-temperature furnace. For KV_6Sb_6 and V_3Sb_2, the furnace was heated from room temperature (RT) to 1073 K in 5 hours, was held at this temperature for 72 hours, and was then allowed to cool naturally back to room temperature. For KV_3Sb_5, a furnace was heated from room temperature (RT) to 873 K in 5 hours, and was held at this temperature for 24 hours, before being cooled down to room temperature. A side reaction of Sb with the Ta tube resulted in the formation of the Ta-Sb binaries as impurities in the thus obtained samples. Therefore, a BN crucible with a lid (OD:7 mm, ID:5 mm, length: 25 mm/30 mm) sealed into a niobium tube was used as an alternative to the sealed Ta tube. The rest of the synthesis steps remained the same. It should be noted that both Nb and Ta tubes are permeable to hydrogen,[66–68] which can eventually escape through the check valve.

Powder X-ray diffraction (PXRD). The purity of synthesized samples and identity of crystalline phases were confirmed by powder X-ray diffraction using a Rigaku MiniFlex600 powder diffractometer with Cu K_α radiation (λ = 1.54051 Å) and Ni K_β filter. Data were collected on a zero-background plate holder in air. For air-sensitive samples, powders were loaded onto non-zero background air-sensitive holders in Ar filled glovebox to avoid oxidation during the PXRD data collection. Phase analysis was performed using the COD database incorporated into the Match-3! Software.[69]

In-situ high-temperature PXRD (HT-PXRD). High-temperature synchrotron X-ray diffraction data were collected at the synchrotron beamline 17-BM at the Advanced Photon Source at Argonne National Lab (APS ANL) at λ = 0.24087 Å. A thick-wall (0.1 mm) silica capillary (0.7 mm outer diameter) was filled with a finely ground sample of KV_6Sb_6 to a height of 10 mm and was flame-sealed under vacuum. The capillary was mounted into a secondary shield capillary located on a sample stage equipped with two resistive micro-heaters and a thermocouple set as close as possible to the measurement area. Data were collected every 1 min upon heating and cooling in the temperature range of 298 K–1245 K–298 K with heating and cooling at a rate of 10 K min^{-1}. Further details of this experimental setup can be found elsewhere.[70]

To study the hydride reaction, the desired molar ratio of KH, V and Sb powders were weighed, and ball milled for 6 minutes in the SPEX mixer/mill 8000M. A silica capillary (dimensions as specified above) was filled with the ball-milled precursors to a height of 10 mm and was sealed under a vacuum at the height of 50 mm to provide enough headspace. This was done to avoid the rupture of the capillary due to over pressurization caused by the release of hydrogen gas during the reaction. Capillary was placed vertically in the X-ray beam during the analysis and PXRD data was collected every 1 min as the sample was heated and cooled at a rate of 20 K/min in the temperature range of 298 K–1173 K–298 K.

Room temperature high-resolution PXRD (HR-PXRD). High-resolution synchrotron powder diffraction data were collected at beamline 11-BM APS ANL at 298 K and λ = 0.45198 Å for a powdered sample of KV_6Sb_6. The sample was loaded into a 0.7 mm outer diameter, thick-wall (0.1 mm) silica capillary that was flame sealed under vacuum. The capillary was placed inside a

Kapton tube, fixed on the mounting base, and covered with a magnetic cap of the sample holder provided by APS ANL.

Structure determination. The program FOX[71] for the *ab initio* structure determination from high-resolution powder X-ray diffraction data was used for indexing and initial structure determination. The powder pattern was indexed as a monoclinic unit cell (a = 9.578082 Å, b = 5.532909 Å, c = 11.868462 Å, β = 105.95 °), space group $C2/m$ (#12), yet the lower symmetry space group $C2$ (#5), which is a subgroup of $C2/m$, was considered for the structure solution. Positions of heavier Sb and V atoms were obtained first: three Sb sites (4*c*, 4*c*, 4*c*) and three V sites (4*c*, 4*c*, 4*c*). In subsequent refinement steps, lighter K atoms were placed in the centers of hexagonal prisms formed by Sb atoms upon consideration of typical coordination environment (2*a* site). Analysis of this model indicated that, indeed, the higher symmetry space group $C2/m$ (initially suggested by FOX) can be considered with K atoms occupying a 2*a* site, Sb atoms occupying three 4*i* sites, and V atoms in 4*i* and 8*j* sites. This model was further refined by the Rietveld method using the JANA 2006 software package,[72] providing a satisfactory fit. Parameters such as preferred orientation, peak shape, background coefficients, lattice parameters, atomic coordinates, atomic displacement parameters and occupancy were refined. This refined model ($C2/m$) was analyzed by Platon[73] for higher symmetry. As a result, a structural model in *R*-rhombohedral unit cell (a = 5.53333 Å, c = 34.2233 Å) in $R\bar{3}m$ (#166) space group was suggested. The structure of KV_6Sb_6 is alike to that of CsV_6Sb_6 and RbV_6Sb_6 compounds[50–53] and was determined independently in this work. The $R\bar{3}m$ model has K atoms in a 3*a* site, V atoms in a 18*h* site, while Sb atoms occupy three 6*c* sites. Details of data collection and refinement are provided in Table S1.[74] Table S2 lists the atomic coordinates, site multiplicity, and atomic displacement parameters (ADP) of all the atomic sites in the structure.[74]

Spark Plasma Sintering: Consolidation of KV_6Sb_6 powder was performed via spark plasma sintering (SPS) using a Dr. Sinter Lab Jr. SPS-211Lx (Sumitomo Coal Mining Co., Ltd.). The powdered sample was loaded into a small graphite die (inner diameter, 5 mm; length, 15 mm) in an argon atmosphere. Two circular graphite foils of 5 mm diameter were placed above and below the powder in the die. Tungsten carbide plungers were inserted on either side of the die to press and hold the powder in place. The assembled smaller die was further inserted into a larger outer graphite die with graphite plungers (inner diameter, 20 mm; length, 40 mm). The samples were sintered by heating to 773 K over a period of 9 minutes under a uniaxial pressure of 117 MPa, followed by dwelling at 773 K for 5 min. Thereafter, the pressure was released, and the sample was allowed to cool to room temperature. In the glovebox the pellets were removed from the graphite die and polished to remove traces of the graphite foil stuck to the pellet surface. The geometrical density of the pellets was measured to be 93–95% of the crystallographic density.

Magnetic property measurement: Magnetic measurement was performed on powders of KV_6Sb_6, V_3Sb_2, and KV_3Sb_5. To avoid oxidation of KV_6Sb_6, a ~50 mg polycrystalline sample was transferred to an EPR tube in an argon-filled glovebox, which was further sealed under a vacuum. V_3Sb_2 and KV_3Sb_5 powders were packed into gel capsules. Measurements were carried out using Quantum Design MPMS XL-7 and MPMS3 SQUID magnetometers. The *dc* magnetic susceptibility measurements were carried out at 0.01T, 0.1 T and 2T constant applied magnetic field in a temperature range of 2–300 K, while the *ac* susceptibility measurements were carried out at a frequency of 100 Hz between 2–50 K (for KV_6Sb_6) and 2–100 K (for KV_3Sb_5) using H_{ac} = 5 Oe.

Thermoelectric properties measurement: Low-temperature transport properties of a KV_6Sb_6 pellet sintered by SPS were measured in a temperature range of 2–300 K using the commercial multipurpose Physical Properties Measurement System Evercool I (PPMS, Quantum Design). The Seebeck coefficient (S) and thermal conductivity (κ) were measured using the thermal transport option in a two-probe configuration. Electrical resistivity (ρ) was measured using the electrical transport option in a four-probe geometric setup, using 50 µm platinum wires attached with silver paste.

Formation energy calculation and heat map construction: An online formation energy predictor tool[64] was utilized for the calculation of the formation energies of various compositions in the K-V-Sb system. This predictor uses a machine learning approach,[64,65] where a large set of data (composition and formation energy), containing output from ~15,000 Density Functional Theory (DFT) calculations for a wide range of chemical systems, is used as input for the predictive model.[65] Formation energies are then predicted for arbitrary compositions independent of structural input using machine learning only, without performing DFT calculations for the selected chemistries. In our work formation energies were calculated for ~1000 $K_xV_ySb_z$ compositions at a 1–2 atomic percent increment. These values were then used to construct a heat map that is a ternary contour plot of formation energy as a function of composition.

Energy Dispersive X-Ray-Scanning Electron Microscopy: Elemental analysis was performed using a JEOL JSM-IT200 scanning electron microscope (SEM) equipped with a JEOL energy-dispersive X-ray (EDX) analysis system with a silicon drift detector. Powder samples and pellets were adhered to aluminum stubs using carbon tape and then placed into an aluminum holder for insertion into the SEM. Samples were oriented perpendicular to the beam and analyzed using a 10–20 kV accelerating voltage with an accumulation time of 60 s.

Differential scanning calorimetry (*DSC):* DSC measurement was performed using a Netzsch 404 F3 Pegasus Differential Scanning Calorimeter. A powdered sample (m = 40 mg) was sealed inside an evacuated silica ampoule, heated to 1173 K, and cooled to 373 K at a rate of 10 K min^{-1}.

Result and discussion.

Synthesis. Interest in ternary alkali metal antimonides containing early 3d metals was sparked with the discovery of the AV_3Sb_5 compounds.[29–33] Flux growth using the low melting eutectic between KSb_2-Sb or KSb_2-KSb and traditional synthesis from elements were employed to synthesize the AV_3Sb_5 compounds.[29] We were interested in further probing the *A*-V-Sb systems using the hydride route, where ductile alkali metal *A* is replaced with its salt-like hydride *A*H. Use of the hydride route allowed for rapid phase screening of various compositions in the K-V-Sb system. The exact composition could be precisely targeted owing to the mixable, salt-like KH precursor as opposed to ductile and soft K metal. Synthesis was guided by *in-situ* studies for fine-tuning the reaction parameters to yield a phase-pure sample of the new KV_6Sb_6 compound, enabling the measurement of magnetic and transport properties.

Initially, the hydride route was utilized to synthesize the previously reported KV_3Sb_5 ternary compound.[29] When precursors mixed in a nominal loading molar ratio of KH:V:Sb = 1:3:5 were heated at 600 °C for 24 hours in a sealed Ta tube, a sample of KV_3Sb_5 was obtained. This validated the use of hydride route to produce crystalline ternary compounds comprising of elements with drastically different reactivities (m.p. K = 337 K, m.p. V = 2183 K, m.p. Sb = 903 K). The use of KH instead of K allowed for shorter milling time (6 mins vs 60 mins) and annealing duration (24 hours vs 48 hours) compared to the previously reported method.[29]

To evaluate the thermal stability of KV_3Sb_5, we collected *in-situ* high-temperature PXRD data for KV_3Sb_5 (Figure 1a). KV_3Sb_5 compound is thermally stable up to 1000 K in a capillary sealed under vacuum. Upon heating above 1000 K, a new set of diffraction peaks were observed around 1073 K (Figure 1a, purple region). This hinted at the existence of a new ternary phase in the system. Figure 1b highlights the 954–1154 K region where the transformation of the KV_3Sb_5 phase to the new ternary phase is observed. Based on this observation, the synthesis temperature for the new phase was kept within the 973–1173 K range.

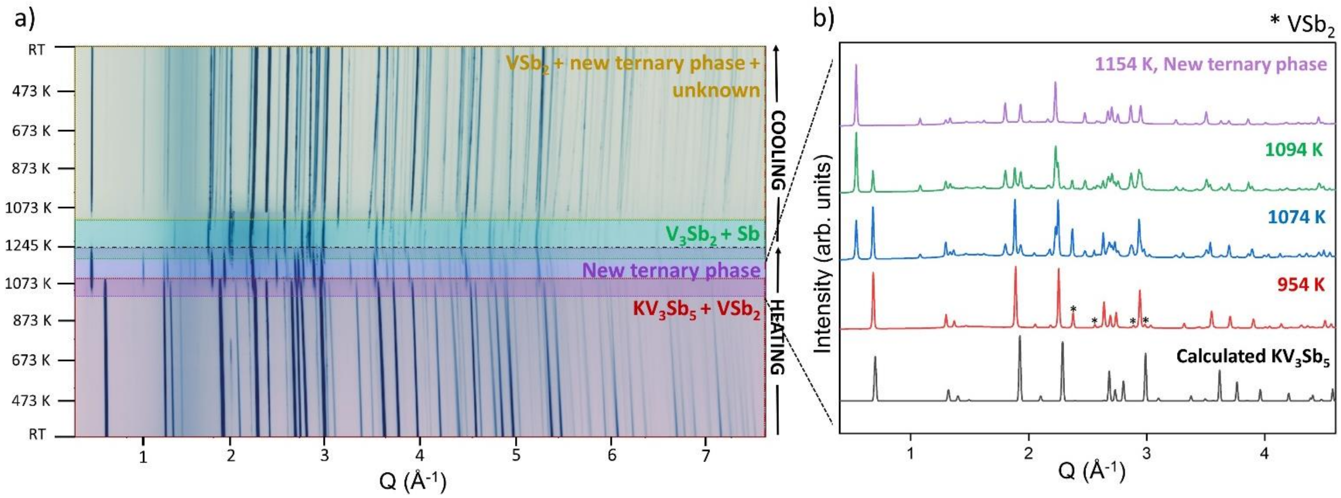

Figure 1. a) High-temperature *in-situ* synchrotron PXRD data for KV_3Sb_5 in the form of a waterfall plot displays sequential changes in the PXRD patterns, collected upon heating and cooling. Each vertical line represents a diffraction peak in the PXRD pattern. Distinct temperature ranges with the indicated phases present are highlighted in red, purple, green, and yellow. b) Selected PXRD patterns in the 954 K–1154 K range indicating the transformation of KV_3Sb_5 into KV_6Sb_6.

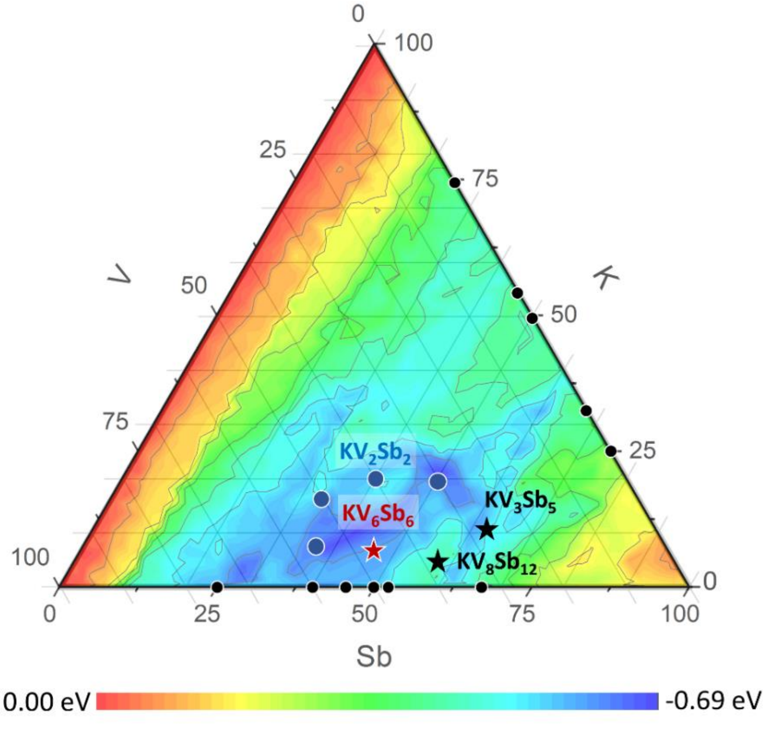

Figure 2. Heat map for the K-V-Sb system. Ternary contour plot of formation energy as a function of compositions calculated using the machine learning approach.[64, 65] The compositions denoted with black stars correspond to ternary compounds reported in the literature for *A*-V-Sb systems (*A* = K, Rb, Cs).[29, 50] The composition denoted with a red star is the one discovered in this work, and blue circles represent other attempted compositions.

With the hints of a new phase and a good estimate of the temperatures to be used for its synthesis, we used a computational heat map of the K-V-Sb system as a guide to narrow down the compositional phase space for further exploration (Figure 2).[64, 65] In a heat map, the compositions that fall into regions of low formation energy are suggestive of a stable compound. For the K-V-Sb system, known phases in the system (i.e., the KV_3Sb_5[29] and KV_8Sb_{12}[50] phases) lie in the negative (low) formation energy region. Based on these predictions, several compositions (represented as blue circles in Figure 2) were attempted in addition to the KV_3Sb_5 stoichiometry. Characteristic diffraction peaks for the new ternary phase were first observed in the sample with a loading molar ratio of KH:V:Sb = 1:2:2 heated at 973 K for 72 hours. The diffraction peaks were broad, signaling low crystallinity of the phase, and were accompanied by the peaks of V_3Sb impurity. This implied a need to tune both the synthesis composition and temperature to obtain a single-phase crystalline sample of the new phase. The SEM-EDX study of the sample with a considerable molar fraction of the new ternary phase revealed the V:Sb ratio to be 1:1. Therefore, when the K content was lowered, maintaining the V:Sb molar ratio at 1:1 (molar ratio of KH:V:Sb = 1.4:6:6) and the synthesis temperature was increased to 1073 K, consistent with high-temperature PXRD data, a crystalline single-phase sample of the target new ternary phase was obtained. Crystal structure solved using high-resolution synchrotron PXRD data determined the new ternary phase to have the composition, KV_6Sb_6 (Figure 3, PXRD pattern in black), which is close to the loading molar ratio of KH:V:Sb = 1.4:6:6.

Note that excess KH with respect to the stoichiometric 1:6:6 composition is required for synthesis and is crucial for preparation of a single-phase sample. As indicated in Figure 3 (PXRD pattern in blue), a nominal composition of KH:V:Sb = 1:6:6 yields the KV_6Sb_6 compound but with broader, unresolved diffraction peaks at $Q \sim 1.8$ Å^{-1}, 3 Å^{-1}, and 3.7 Å^{-1} highlighted in yellow (Figure 3). The diffraction peaks remain to be broad even after the second annealing as seen in Figure S1a.[74] In fact, the formation of the KV_6Sb_6 is extremely sensitive to the amount of K loaded for the reaction. Figure S1a shows the PXRD data for reactions with variation in KH content, i.e., $K_{1+x}V_6Sb_6$ (x = 0, 0.2, 0.4 and 0.6).[74] With an increase in K content, the diffraction peaks at $Q \sim 1.8$ Å^{-1}, 3 Å^{-1}, and 3.7 Å^{-1} (highlighted in yellow in in Figure S1a[74] and Figure 3) appear well-resolved. With a decrease in the K content, an additional peak appears between the highlighted set of two peaks (making them appear broader and unresolved), suggesting formation of a structurally related phase with reduced K content, i.e., $K_{1-y}V_6Sb_6$.[74] The difference in the intensity between observed and calculated diffraction peaks at Q ~ 0.6 Å^{-1} (highlighted in blue, Figure 3) is attributed to preferred orientation in the sample. Refer to Figure S2 for further details.[74]

To prove that KV_6Sb_6 is not an H-stabilized phase, reactions were carried out with K metal under identical reaction conditions. Indeed, the KV_6Sb_6 phase forms albeit along with a KV_3Sb_5 impurity (Figure S1b).[74] We hypothesize that the use of elemental K instead of the hydride does not allow for sufficient initial mixing of the precursors. Thus, the synthesis proceeds with diffusion limitation through the formation of more K-rich and Sb-rich KV_3Sb_5 ternary phase first, resulting in a multiphase sample even under identical reaction conditions. There is no variation in unit cell parameters (within e.s.d.) for KV_6Sb_6 prepared using elemental K or KH, suggesting that H is not incorporated in the interstitial sites of KV_6Sb_6 and that KV_6Sb_6 prepared from KH is not H-stabilized. Additionally, our previous work on other alkali-metal-containing ternary antimonides shows no evidence of hydrogen incorporation when an alkali metal hydride is used as a precursor.[61, 63] Nevertheless, the synthesis of KV_6Sb_6 using elemental K results in a PXRD pattern with well-resolved set of two peaks at Q ~ 1.8 Å^{-1}, 3 Å^{-1}, and 3.7 Å^{-1} (Figure S1b),[74] compared to KV_6Sb_6 synthesized using KH.

In summary, the hydride route in tandem with *in-situ* studies and computationally predicted stable ternary compositions allowed for the optimization of synthesis conditions for fast synthesis of a high-purity polycrystalline sample of the title compound.

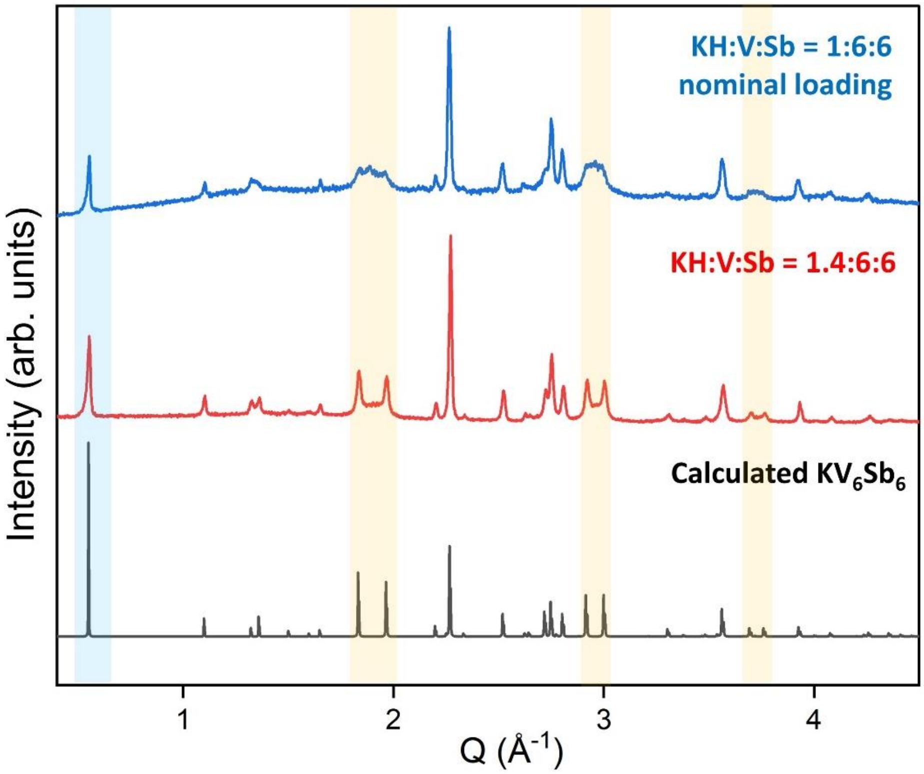

Figure 3. Experimental powder X-ray diffraction pattern for sample synthesized with KH:V:Sb = 1.4:6:6 and KH:V:Sb = 1:6:6 loading molar ratio, signifying a difference in crystallinity with K content. The yellow shaded region highlights the difference in crystallinity for the set of two peaks and blue region highlights the preferred orientation.

To further study the kinetics of the KV_6Sb_6 formation using KH, we collected *in-situ* high temperature PXRD data upon heating of KH, V and Sb powders mixed in a 1.3:6:6 molar ratio (Figure 4). Initially, at room temperature, only diffraction peaks for Sb are seen in the PXRD data since Sb is the strongest scatterer of X-rays of the three components (KH, V and Sb). As the temperature approaches the melting point of Sb (903 K), diffraction peaks for V become visible at ~650 K along with a simultaneous decrease in intensity of diffraction peaks for Sb, suggesting the onset of Sb melting. Further heating the mixture to 850 K promotes reaction of the starting elements, leading to the formation of VSb_2 and KV_3Sb_5. This matches well with the synthesis temperature of 873 K for KV_3Sb_5.[29] There is no clear indication of the formation of K-Sb binaries in the given temperature range. Above 850 K, KV_3Sb_5 transforms to KV_6Sb_6, with KV_6Sb_6 becoming the major phase at 1073 K. It remains the major phase down to room temperature upon cooling.

The temperature range over which the formation of the KV_6Sb_6 occurs is in good agreement with the *in-situ* study on the KV_3Sb_5 compound (Figure 1), supporting the earlier choice of synthesis temperature. The reaction is rapid because of the intimate mixing of precursors allowing to monitor reaction progress with *in-situ* X-ray diffraction. KV_3Sb_5 forms first at low temperatures and acts as an intermediate that transforms to KV_6Sb_6 at higher temperatures. Based on the *in-situ* study, the reaction mechanism can be roughly represented as: KH + V + Sb → VSb_2 + melt → KV_3Sb_5 + melt → KV_6Sb_6. Overall, the *in-situ* study provided insights into the reaction mechanism and confirms the viability of utilizing KH for the synthesis of the KV_6Sb_6 phase.

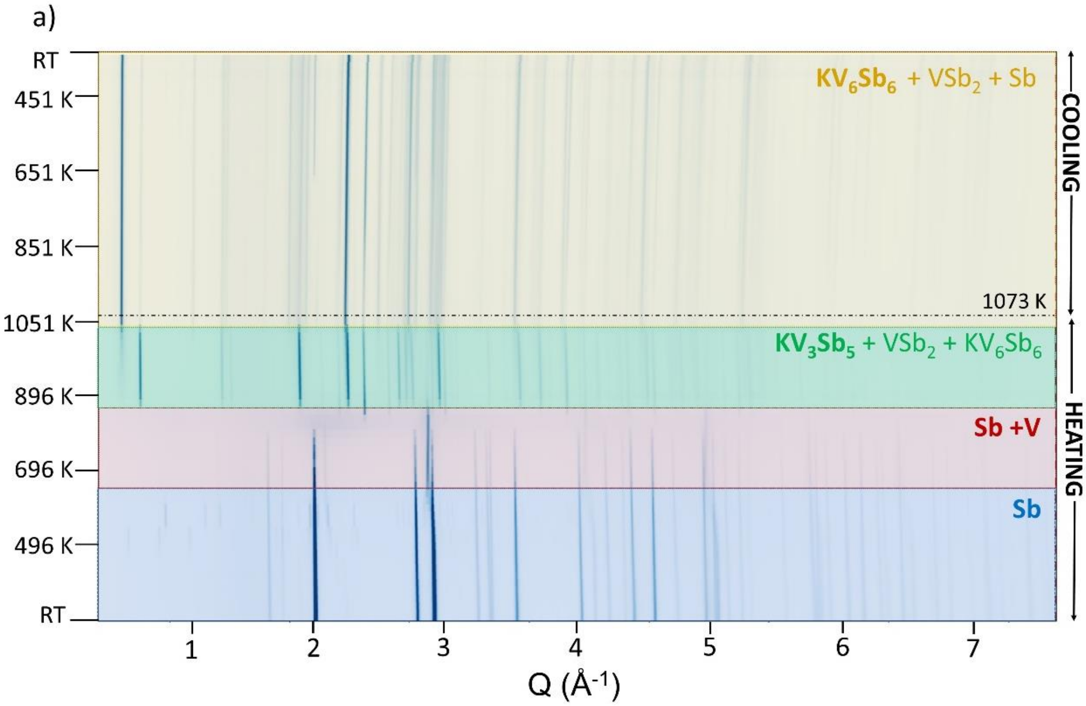

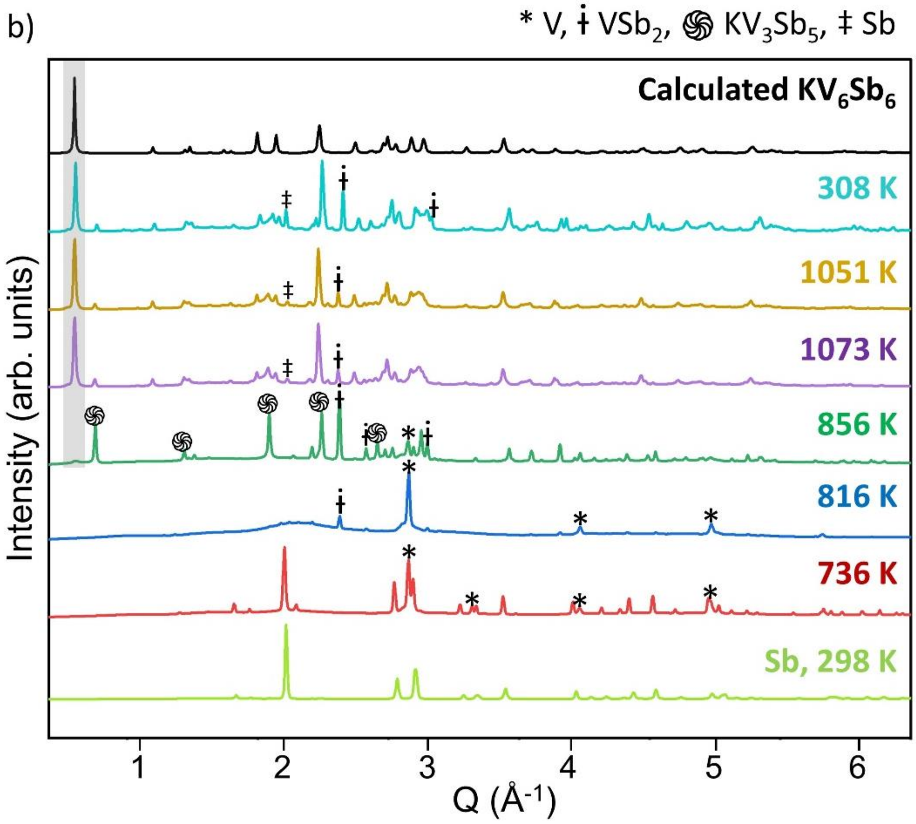

Figure 4. a) High-temperature *in-situ* synchrotron PXRD data for the hydride reaction in the form of a waterfall plot displays sequential changes in the PXRD patterns, collected upon heating and cooling. Each vertical line represents a diffraction peak in the PXRD pattern. Distinct temperature ranges with the indicated phases present are highlighted in blue, red, green, and yellow. b) Selected PXRD patterns showing the formation of KV_6Sb_6 through the identified crystalline intermediates.

Composition and thermal stability. Using EDX-SEM analysis, the composition of the novel phase was found to be $K_{1.3(1)}V_{6.1(1)}Sb_{6.0(2)}$, which is close to the composition of the compound obtained from PXRD data. Analysis was performed on a flat surface of an SPS-sintered pellet with 95% compactness. The sintering of the pellet for EDX-SEM analysis was accomplished under the same conditions as the pellet used for the measurement of transport properties (93% compactness). As evident from Figure S3,[74] sintering leads to a well-consolidated pellet and an even distribution of K, V and Sb across the entire sample.

To study the thermal stability of KV_6Sb_6, *in-situ* high temperature synchrotron PXRD data was collected on a sample of KV_6Sb_6 containing minor V_3Sb impurity in the temperature range of RT–

1173 K (Figure S4).[74] As seen in Figure S4a, KV_6Sb_6 is thermally stable up to 1173 K. This is consistent with DSC data (Figure S5),[74] as no thermal events were observed during the heating and the cooling cycles. Figure S4b shows selected PXRD patterns from the *in-situ* high-temperature synchrotron PXRD study, underlining the phase transformations over the temperature range.[74] KV_6Sb_6 is the major phase at all measured temperatures during the heating cycle. At ~500 K during heating, the diffraction peaks of elemental Sb start to appear along with a slight increase in the intensity of diffraction peaks for the V_3Sb. We hypothesize that upon heating, a small fraction of K is "leached" from the KV_6Sb_6 phase due to a side reaction with the silica capillary (in which the sample is sealed), leading to the formation of the V_3Sb and Sb. At ~773 K we see the simultaneous appearance of the KV_3Sb_5 phase and the disappearance of Sb and V_3Sb. This might be a result of the reaction between KV_6Sb_6, V_3Sb and Sb to form the comparatively Sb-rich, KV_3Sb_5 ternary phase. As the sample is heated above 1073 K, KV_3Sb_5 transforms back into KV_6Sb_6, in accordance with the findings of the *in-situ* PXRD study for the KV_3Sb_5 compound (Figure 1) and the mechanistic study of the hydride reaction (Figure 4). From the *in-situ* studies, it can be concluded that the synthesis of the KV_6Sb_6 should be carried out at T ~ 1073 K to avoid the formation of the competing ternary phase. Upon cooling, elemental Sb crystallizes at ~873K (m.p. 903 K) and the Sb fraction gradually increases as the sample is cooled down to room temperature. This study indicates that KV_6Sb_6 is thermally stable up to 1173 K.

To summarize, high temperature *in-situ* studies have been vital in the discovery and study of the new KV_6Sb_6 compound: first, hinting at the existence of the title compound, then helping to pinpoint an appropriate synthesis temperature, offering insight into the reaction mechanism, and establishing the thermal stability of the compound.

Crystal structure. Since hydride synthesis yields microcrystalline powders with crystals too small for single crystal X-ray diffraction study, the crystal structure of the KV_6Sb_6 phase was solved from high-resolution synchrotron PXRD data using FOX[71] and refined using JANA 2006 packages.[72] As described in the experimental part, indexing the peaks initially yielded a monoclinic $C2/m$ unit cell, which on further refinement and analysis led to a rhombohedral $R\overline{3}m$ model for the KV_6Sb_6 compound. Parameters including lattice parameters, atomic coordinates, preferred orientation, site occupancy and isotropic displacement parameters were refined. The calculated PXRD patterns for the two models were compared to the experimental high-resolution PXRD data for the phase (Figure S6).[74] The two models closely resemble each other except for the splitting of certain peaks (Figure S6).[74] Upon solving the structure of KV_6Sb_6, we became aware of the report on the isostructural compounds RbV_6Sb_6 and CsV_6Sb_6.[44–47] The increase in *c* parameter as the size of alkali metal cation increases (34.23 Å for K, 34.61 Å for Rb and 35.28 Å for Cs) follows the expected trend while the variation in *a* parameter ($a(KV_6Sb_6)$= 5.53 Å, $a(RbV_6Sb_6)$ = 5.51 Å and $a(CsV_6Sb_6)$ = 5.51 Å) is minor, leading to an overall increase in the unit cell volume. Careful analysis of the residual curve from the Rietveld refinement (Figure S6b)[74] indicated additional diffraction intensity between the (107) and (108) peaks at $Q \sim 1.8$ Å^{-1}, (207) and (208) at $Q \sim 3.0$ Å^{-1}, and (217) and (218) peaks at $Q \sim 3.7$ Å^{-1} (black arrows in Figure S6b) as well as a positive difference between $I_{obs} - I_{calc}$ for peaks with (003), (006), (0015), (110), (1115) *hkl* indices (red arrows in Figure S6b), resulting in relatively high *R*-values for the fit. We hypothesize that the proposed rhombohedral model does not fully capture the complexity of KV_6Sb_6 structure. The deviations between experimental and refined PXRD patterns could be attributed to the beginning of deintercalation of K^+ ions from the layers to form a related $K_{1-y}V_6Sb_6$ phase, as discussed earlier (Figure S1 and Figure 3) or could be due to inherent stacking faults in the layered structure that would cause discrepancies in diffraction intensity, leading to the unusual broadening of peaks even in the high resolution PXRD data. Nonetheless, we believe that the $R\overline{3}m$ model provides an acceptable fit of the PXRD data and is a plausible structural solution for the title compound.

The rhombohedral structure of the KV_6Sb_6 compound consists of $[V_6Sb_6]^-$ layers alternating with K^+ layers (Figure 5). There is one atomic site for K, one for V atoms and three unique Sb atomic sites, Sb(1), Sb(2) and Sb(3). A single $[V_6Sb_6]$ layer can be represented as $[Sb_2]$-$[V_3Sb]$-$[V_3Sb]$-$[Sb_2]$, i.e., a double layer of $[V_3Sb]$ capped by single layers of Sb atoms from either side (Figure 5a). Within the $[V_6Sb_6]$ blocks, the Sb(1) and V atoms appear in the $[V_3Sb]$ layers, whereas Sb(2) and Sb(3) atoms constitute the capping layers. V atoms in the structure form a Kagome network with a V-V distance of 2.776 Å, while the Sb(2) and Sb(3) atoms in the capping layers form a hexagonal network with Sb2-Sb3 distance of 3.129 Å (Figure 5b). The Sb(1) atoms are also arranged in a hexagonal pattern in the structure with an Sb1-Sb1 distance of 5.532 Å. Figure 5d shows the

$[V_6Sb_6]$ layer of KV_6Sb_6, highlighting the stacking of the V and Sb networks along the [001] direction. Layers are shifted with respect to one another as they stack along the [001] direction.

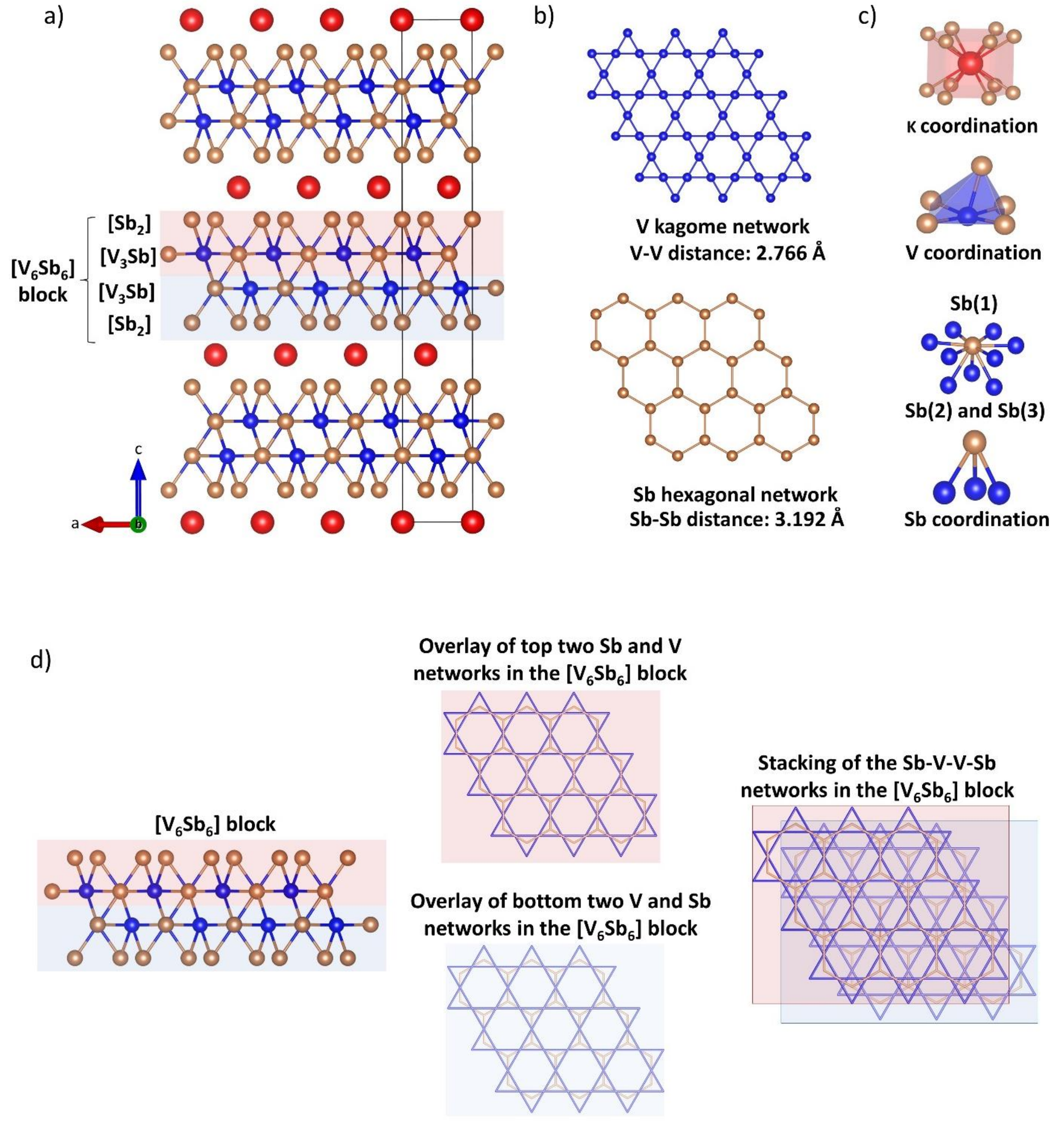

Figure 5. Crystal structure of KV_6Sb_6 [red: K, blue: V and Gold: Sb] highlighting a) the layered structure, b) V and Sb networks, c) coordination environments of the K, V and Sb atoms and d) stacking of Sb and V networks in the $[V_6Sb_6]$ block.

The structure of KV_6Sb_6 displays remarkable similarities with the crystal structure of V_3Sb_2, a compound that also crystallizes in the rhombohedral space group $R\overline{3}m$ (Figures 6a-b). The structure of the KV_6Sb_6 ternary phase can be viewed as a derivative of the V_3Sb_2 structure where two adjacent [V_3Sb] layers are "stripped" and replaced by a single layer of K^+ (Figures 6a-b). The two compounds have identical [V_6Sb_6] layers (shaded in light blue in Figure 6a-b). The V atoms in both compounds are coordinated to Sb atoms to form a distorted square pyramid (Figure S7).[74] Sb shows similar coordination environments in V_3Sb_2 and KV_6Sb_6 (Figure S7).[74]

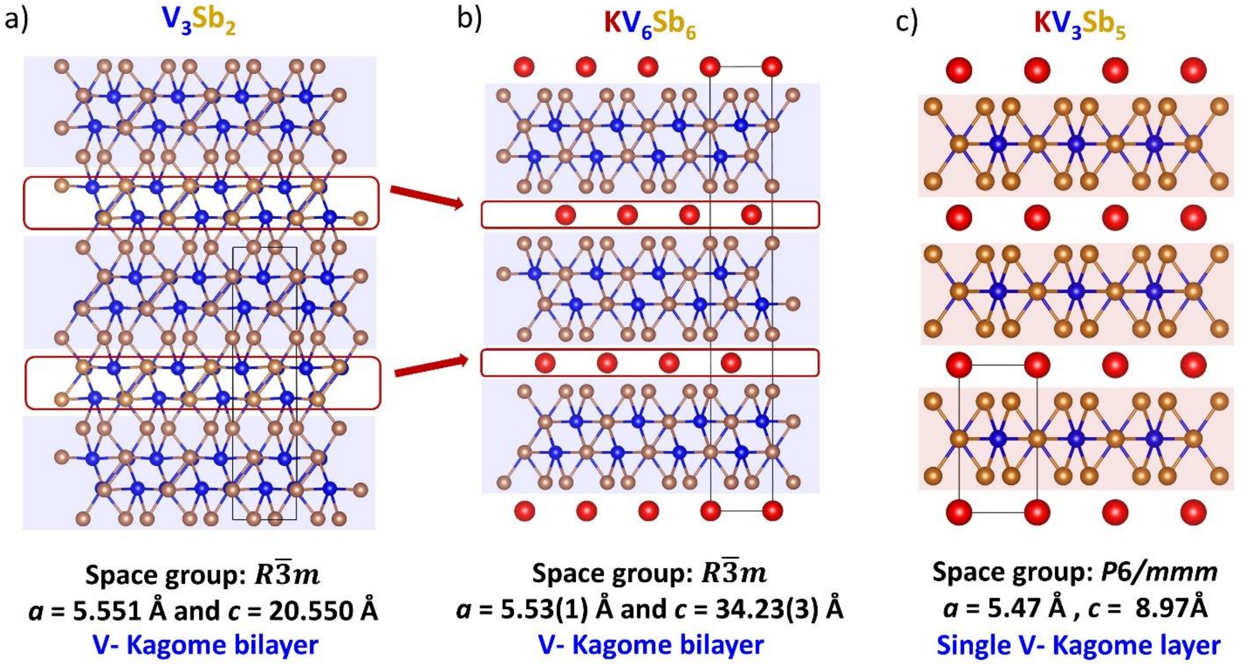

Figure 6. Comparison of V_3Sb_2, KV_6Sb_6 and KV_3Sb_5 crystal structures.

Figure 6 also illustrates how the structure of KV_6Sb_6 is similar to that of KV_3Sb_5.[29] Both compounds have a layered structure. The KV_3Sb_5 compound crystallizes in the hexagonal space group $P6/mmm$ and hence has a more symmetric arrangement of atoms in the unit cell compared to KV_6Sb_6. This is also reflected in the change in the coordination environment of the V and the Sb atoms (Figure S7).[74] The major difference between the two structures is the single layer of the V Kagome network in KV_3Sb_5 as compared to the V Kagome bilayers in KV_6Sb_6 and V_3Sb_2. In fact, KV_6Sb_6 and KV_3Sb_5 have similar layered structures with an extra layer of "V_3Sb" in KV_6Sb_6 (Figure

6b-c). In summary, KV_6Sb_6 has structural features strikingly similar to those of V_3Sb_2 and KV_3Sb_5. Band structure calculations for KV_6Sb_6 reported elsewhere[51,52] suggest a metallic behavior for the compound, which would mean that KV_6Sb_6 is not a classical, charge balanced Zintl phase.[75,76]

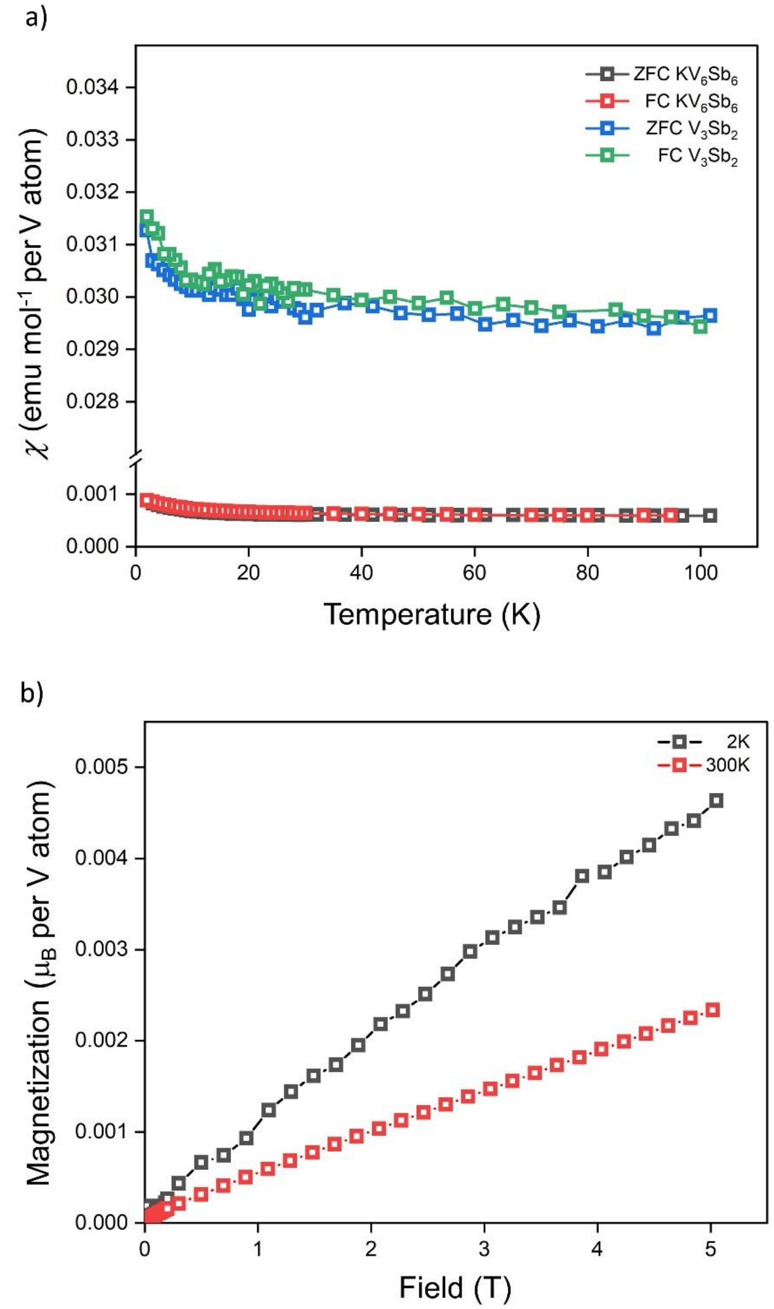

Figure 7. Magnetic properties of the structurally related KV_6Sb_6 and V_3Sb_2 phases: a) ZFC/FC magnetic susceptibility (χ) per V atom as a function of temperature for KV_6Sb_6 and V_3Sb_2 measured in the applied field of 0.1 T; b) Magnetization per V atom for KV_6Sb_6 as a function of magnetic field at 2 K and 300 K.

Magnetic and transport properties. As discussed in the previous section, the KV_6Sb_6 compound is structurally similar to V_3Sb_2 and KV_3Sb_5 and features a Kagome lattice of V atoms. With the recent discovery of superconductivity in the AV_3Sb_5 (A = K, Rb, Cs) family of compounds,[29–33] we examined the magnetic properties of KV_6Sb_6. Due to their structural similarities, we also compared the magnetic properties of KV_6Sb_6 with those of V_3Sb_2 and KV_3Sb_5.

Figure 7a represents a plot of molar *dc* magnetic susceptibility (χ) per V atom as a function of temperature for KV_6Sb_6 and V_3Sb_2, measured at 0.1 T applied magnetic field. The data reveals temperature-independent (Pauli) paramagnetism for both KV_6Sb_6 and V_3Sb_2 with no splitting of the zero-field cooling (ZFC) and field cooling (FC) curves. There is a slight upturn of magnetic moment at lower temperatures ($T < 10$K). The temperature dependence of χ for KV_6Sb_6 is similar to that of the isostructural RbV_6Sb_6 and CsV_6Sb_6 phases.[50–53] The paramagnetic behavior in KV_6Sb_6 is evident from the linear trend of magnetization *vs.* applied field for $M(H)$, collected at both 2 K and 300 K (Figure 7b). The deviations from linearity in $M(H)$ at 2 K for V_3Sb_2 (Figure S8)[74] suggest a ferromagnetic contribution, but given the small value of saturation magnetization, this feature is likely not intrinsic to the V_3Sb_2 phase and might stem from ferromagnetic impurities. The magnetic susceptibility χ per V atom is more than an order of magnitude higher for V_3Sb_2 than for KV_6Sb_6. We found no evidence of superconductivity in KV_6Sb_6 down to 2 K from either of these data sets or the *ac* susceptibility measurements (Figure S9).[74] Even though AV_6Sb_6 (A = K, Rb, Cs) compounds are not superconducting at ambient pressure, superconductivity can be induced by strong applied hydrostatic pressures ($T_{c,max}(KV_6Sb_6) = 0.37$ K at 31 GPa, $T_{c,max}(RbV_6Sb_6) = 1.36$ K at 28 GPa, $T_{c,max}(CsV_6Sb_6) = 1.48$ K at 33 GPa).[52]

We also compared the low-temperature magnetic properties of the polycrystalline KV_3Sb_5 sample synthesized via the hydride route with that of the polycrystalline KV_3Sb_5 sample prepared via a traditional route from elements in the study by Ortiz, *et. al.*[29] (see Figure S10-11 and discussion in the Supporting Information).[74] Briefly, the magnetic properties of KV_3Sb_5 compound synthesized via the new hydride route are consistent with paramagnetic behavior and low magnetic moment per V atom previously observed.[29] The parameters of Curie-Weiss fit are consistent with the previous study[29] with the exception of Weiss temperature. However, the "anomaly" at 80 K observed in both magnetization and heat-capacity measurements for the

KV_3Sb_5 sample synthesized via the traditional route from elements[29] is not seen for the KV_3Sb_5 sample synthesized via the hydride route (Figure S11).[74] The Curie-Weiss fit of the FC susceptibility curve for KV_6Sb_6 shown in Figure S12, reveals comparable values of the fit parameters for the KV_6Sb_6 and KV_3Sb_5 phases. Details of the fitting and the values of the parameters can be found in Figure S12 of the Supporting Information.[74]

Given that KV_6Sb_6 belongs to the family of ternary antimonides with a layered structure, we were interested in measuring the thermoelectric properties of KV_6Sb_6. Among the layered antimonides, AM_2Sb_2 Zintl compounds (A = Ca, Sr, Ba, Eu, Yb and M = Zn, Cd) boast excellent thermoelectric properties.[78,79,81–84] Thermoelectric materials are characterized by the unitless figure of merit $zT = S^2T/\rho\kappa$, where S is the Seebeck coefficient; ρ is the electrical resistivity; and κ is the thermal conductivity. For decent thermoelectric performance, the zT needs to be as high as possible and for practical applications should exceed 1.[77] In the AM_2Sb_2 family, the $YbCd_2Sb_2$ compound has been reported to have zT = 1.0 at 675 K.[78,79] The Mn doped variants of $YbCd_2Sb_2$ also display $zT > 1$ in the moderate temperature range.[79]

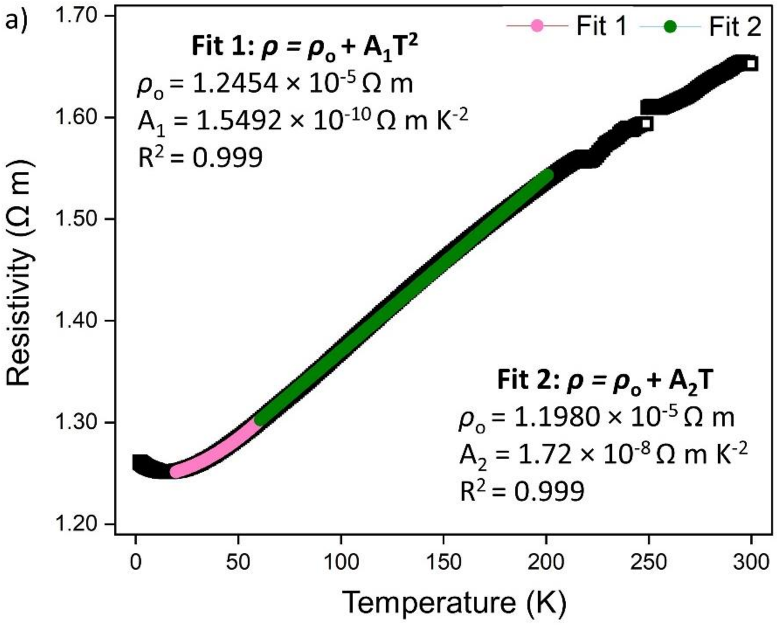

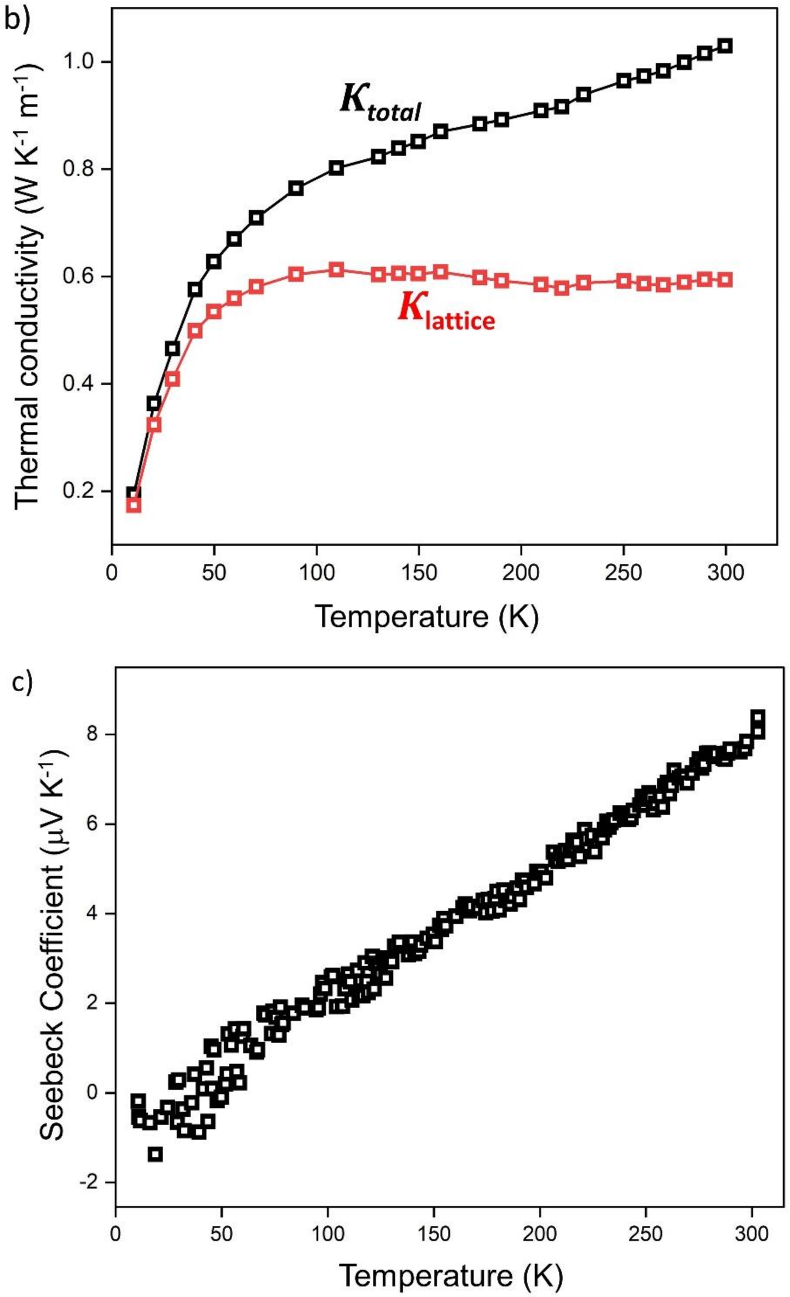

Figure 8. Transport properties of KV_6Sb_6 phases as a function of temperature: a) Electrical resistivity, *ρ*, b) thermal conductivity, *K*, and c) Seebeck coefficient, *S.* The variation in resistivity in the 200-250 K range is not due to a phase transition but is attributed to the loose electrical contact.

Measurements of low-temperature electrical and thermal transport properties of KV_6Sb_6 (Figure 8) were performed using an SPS-consolidated pellet with 93% compactness. Electrical resistivity *ρ* increases with an increase in temperature, indicating metallic behavior (Figure 8a). The values of ρ in the 5–300 K range ($1.25 \times 10^{-5} - 1.65 \times 10^{-5}$ Ω m) are typical for a metal. The resistivity reported earlier for the KV_6Sb_6 phase in the same temperature range is $0.25 \times 10^{-5} - 0.45 \times 10^{-5}$ Ω m,[52] which is on the same order of magnitude as the resistivity values obtained in this work. The $\rho = \rho_o + AT^2$ parabolic model provided a good fit of the resistivity data in the low-temperature range of 20 – 60 K, indicating that at low temperatures, electron-electron scattering dominates. The model gave the value of parameter $A = 1.5 \times 10^{-10}$ Ω m K^{-2} for KV_6Sb_6 comparable to the A parameter of KV_3Sb_5 phase (3.0×10^{-10} Ω m K^{-2}).[29] In the higher temperature range of 60–200 K, resistivity has a linear dependence on temperature. The data can be fit using the $\rho = \rho_o + AT$ model, in accordance with the electron-phonon scattering at high temperatures in a metal. We hypothesize that the upturn in resistivity below 20 K is due to imperfections in the crystal structure, such as vacancies and stacking faults, since the resistivity measured on the flux grown KV_6Sb_6 single crystal lacks such low-temperature feature.[52]

The metallic nature of KV_6Sb_6 is in line with the low values of the Seebeck coefficient S, which reaches 8.5 μV K^{-1} at 300 K (Figure 8b). Positive values of S suggest holes as charge carriers. The total thermal conductivity (κ_{total}) for KV_6Sb_6 is unusually low for a metallic compound and close to typical values for a glass (1.2 W K^{-1} m^{-1} at 300 K) (Figure 8c). The value of κ_{total} also resembles those for clathrates and layered antimonides studied for thermoelectric applications.[77,80,81] Electronic contribution to κ_{total} ($\kappa_{el} = L\sigma T = LT/\rho$, $L = 2.4 \times 10^{-8}$ W Ω K^{-2}) is significant (~50% at 300 K), suggesting intrinsically low lattice thermal conductivity ($\kappa_{\mathrm{lattice}}$) for KV_6Sb_6. The comparison of thermal conductivity values at 300 K (Table 1) shows that the κ_{total} of KV_6Sb_6 is on par with other layered ternary antimonides. The figure of merit for the KV_6Sb_6 compound zT is low (0.001 at 300 K), arising from the low Seebeck coefficient. With an intrinsically low κ, doping can be attempted to increase the S values of KV_6Sb_6 to improve the thermoelectric performance. KV_6Sb_6 has a layered structure with fairly independent ionic (K^+ layers) and covalent fragments (V_6Sb_6 layers), potentially allowing for the alteration of the electronic structure via doping to improve the TE properties. Moreover, the high-temperature thermoelectric properties of KV_6Sb_6 should be a subject of future investigation given the exceptional thermal stability of KV_6Sb_6 up to ~1200 K.

Table 1. Total thermal conductivity (K_{total}) and room-temperature figure of merit zT for some layered antimonides.

Compound	**K_{total} at 300 K ($W\ K^{-1}\ m^{-1}$)**	**zT at 300 K**
KV_6Sb_6 $^{\text{this work}}$	1.00	0.001
Mg_3Sb_2[82]	1.35	0.002
$YbCd_2Sb_2$[78,79]	2.20	0.145
$EuCd_2Sb_2$[78]	1.35	0.125
$CaZn_2Sb_2$[83]	2.20	0.075
$YbCd_{1.6}Mn_{0.4}Sb_2$[79]	1.10	0.140
$Ca_{0.5}Yb_{0.5}Zn_2Sb_2$[84]	1.00	0.100

Conclusion.

The hydride synthesis route guided by *in-situ* powder X-ray diffraction and computationally predicted stable compositions in the K-V-Sb system led to the discovery of the new KV_6Sb_6 phase. *In-situ* powder X-ray diffraction study highlighted the thermal stability of the compound up to 1173 K. Additionally, *in-situ* study aided the elucidation of the reaction mechanism when using a hydride precursor: the formation of the title compound proceeds via the formation of the intermediate ternary KV_3Sb_5, which eventually transforms to KV_6Sb_6 upon further heating. The KV_6Sb_6 compound is isostructural to RbV_6Sb_6 and CsV_6Sb_6 phases and crystallizes in $R\bar{3}m$ layered structure that consists of alternating K^+ and $[V_6Sb_6]$ layers. Within the $[V_6Sb_6]$ layer, V atoms form Kagome bilayers, while Sb atoms form a graphene-like hexagonal net. PXRD data indicate a clear tendency for K to move out of the layers, altering the PXRD pattern and making this compound a candidate for deintercalation studies to further alter its transport properties. The KV_6Sb_6 compound displays temperature-independent paramagnetic behavior and lacks superconductivity above 2 K at ambient pressure, similar to the Rb and Cs analogs. KV_6Sb_6 is metallic, with low positive values of Seebeck coefficient and intrinsically low total thermal conductivity of 1.0 W K^{-1} m^{-1} at 300 K. Doping or K^+ ions deintercalation from the KV_6Sb_6 crystal structure can pave the way for optimized thermoelectric properties by modification of its electronic structure.

Through this work, we have expanded the family of Kagome compounds in the *A*-V-Sb system by utilizing compositional screening via hydride synthesis. Hydride synthesis presents an alternative method for the preparation of ternary compounds in the K-V-Sb and similar systems, offering advantages such as thorough mixing of precursors to overcome diffusion barriers, lower synthesis temperature, and shorter synthesis time. Hydride synthesis combined with *in-situ* diffraction and machine learning capabilities to rapidly optimize reaction temperatures and composition offers an effective strategy for the discovery of new compounds with potentially remarkable properties and can be extended toward other systems with early 3d transition metals.

Acknowledgements.

Financial support from the National Science Foundation (DMR-1944551) CAREER award is gratefully acknowledged. The magnetic measurements were supported by the Division of Materials Science and Engineering of the Office of Basic Energy Sciences, Office of Science of the U. S. Department of Energy (DOE) through the Ames National laboratory. Ames National Laboratory is operated for the US Department of Energy by Iowa State University under contract DE-AC02-07CH11358. Use of the Advanced Photon Source at Argonne National Laboratory was supported by the U. S. Department of Energy, Office of Science, Office of Basic Energy Sciences, under contract no. DE-AC02-06CH11357. Dr. Wenqian Xu and Dr. Andrey Yakovenko at 17-BM are acknowledged for helping with high-temperature synchrotron powder XRD data collection and Dr. Saul Lapidus at 11-BM beamline APS ANL for his help with high-resolution powder XRD data collection. We thank Dr. Kirill Kovnir (Chemistry Department, Iowa State University and US-DOE Ames Laboratory) for the access to DSC-TG and PPMS and Dr. Warren Straszheim (Materials Analysis Research Laboratory, Iowa State University) for the help with SEM/EDXS data acquisition.

References:

1. S. K. Pati, and C. N. R. Rao, Kagome network compounds and their novel magnetic properties, Chem. Commun., 4683 (2008).

2. M. Jovanovic, and L. M. Schoop, Simple Chemical Rules for Predicting Band Structures of Kagome Materials, J. Am. Chem. Soc. 124, 10978 (2022).

3. V. Meschke, P. Gorai, V. Stevanovic, and E. S. Toberer, Search and Structural Featurization of Magnetically Frustrated Kagome Lattices, Chem. Mater. 33, 4373 (2021).

4. J. R. Chamorro, T. M. McQueen, and T. T. Tran, Chemistry of quantum spin liquids, Chem. Rev. 121, 2898 (2020).

5. L. Balents, Spin liquids in frustrated magnets, Nature 464, 199 (2010).

6. M. Sinha, H. K. Vivanco, C. Wan, M. A. Siegler, V. J. Stewart, E. A. Pogue, L. A. Pressley, T. Berry, Z. Wang, I. Johnson, M. Chen, T. T. Tran, W. M. Phelan, and T. M. McQueen, Twisting of 2D kagomé sheets in layered intermetallics, ACS Cent. Sci. 7, 1381 (2021).

7. M. R. Norman, Colloquium: Herbertsmithite and the search for the quantum spin liquid, Rev. Mod. Phys. 88, 041002 (2016).

8. S. Lucile, and L. Balents, Quantum spin liquids: a review, Rep. Prog. Phys. 80, 016502 (2016).

9. J. E. Greedan, Geometrically frustrated magnetic materials, J. Mater. Chem. 11, 37 (2001).

10. D. Grohol, D.G. Nocera, and D. Papoutsakis, Magnetism of pure iron jarosites, Phys. Rev. B 67, 064401 (2003).

11. C. N. R. Rao, E. V. Sampathkumaran, R. Nagarajan, G. Paul, J. N. Behera, and A. Choudhury, Synthesis, structure, and the unusual magnetic properties of an amine-templated iron (II) sulfate possessing the Kagome lattice, Chem. Mater. 16, 1441 (2004).

12. D. G. Nocera, B. M. Bartlett, D. Grohol, D. Papoutsakis, and M. P. Shores, Spin frustration in 2D kagomé lattices: A problem for inorganic synthetic chemistry, Chem. Eur. J. 10, 3850 (2004).

13. R. A. Klein, J. P. S. Walsh, S. M. Clarke, Y. Guo, W. Bi, G. Fabbris, Y. Meng, D. Haskel, E. E. Alp, R. P. Van Duyne, S. D. Jacobsen, and D. E. Freedman, Impact of pressure on magnetic order in jarosite, J. Am. Chem. Soc. 140, 12001 (2018).

14. R. A. Klein, J. P. S. Walsh, S. M. Clarke, Z. Liu, E. E. Alp, W. Bi, Y. Meng, A. B. Altman, P. Chow, Y. Xiao, M.R. Norman, J. M. Rondinelli, S. D. Jacobsen, D. Puggioni, and D. E. Freedman, Pressure-Induced Collapse of Magnetic Order in Jarosite, Phys. Rev. Lett. 125, 077202 (2020).

15. M. A. Subramanian, G. Aravamudan, and G. V. Subba Rao, Oxide pyrochlores—a review, Prog. Solid State Chem. 15, 55 (1983).

16. M. P. Zinkin, M. J. Harris, and T. Zeiske, Short-range magnetic order in the frustrated pyrochlore antiferromagnet $CsNiCrF_6$, Phys. Rev. B 56, 11786 (1997).

17. M. Enjalran, M. J. P. Gingras, Y. J. Kao, A. Del Maestro, and H. R. Molavian, The spin liquid state of the $Tb_2Ti_2O_7$ pyrochlore antiferromagnet: a puzzling state of affairs, J. Phys.: Condens. Matter 16, S673 (2004).

18. R. Moessner, and A. P. Ramirez, Geometrical frustration, Phys. Today 59, 24 (2006).

19. M. P. Shores, E. A. Nytko, B. M. Bartlett, and D. G. Nocera, A structurally perfect S = ½ Kagomé antiferromagnet, J. Am. Chem. Soc. 127, 13462 (2005).

20. R. Sibille, E. Lhotel, M. C. Hatnean, G. Balakrishnan, B. Fåk, N. Gauthier, T. Fennell, and M. Kenzelmann, Candidate quantum spin ice in the pyrochlore $Pr_2Hf_2O_7$, Phys, Rev. B, 94, 024436 (2016).

21. L. Opherden, J. Hornung, T. Herrmannsdörfer, J. Xu, A. T. M. N. Islam, B. Lake, and J. Wosnitza, Evolution of antiferromagnetic domains in the all-in-all-out ordered pyrochlore Nd2Zr2O7, Phys. Rev. B 95, 184418 (2017).

22. J. D. Thompson, P. A. McClarty, D. Prabhakaran, I. Cabrera, T. Guidi, and R. Coldea, Quasiparticle breakdown and spin Hamiltonian of the frustrated quantum pyrochlore $Yb_2Ti_2O_7$ in a magnetic field, Phys. Rev. Lett. 119, 057203 (2017).

23. T. A. Bojesen, and S. Onoda, Quantum spin ice under a [111] magnetic field: from pyrochlore to kagome, Phys. Rev. Lett. 119, 227204 (2017).

24. E. Lhotel, S. Petit, M. Ciomaga Hatnean, J. Ollivier, H. Mutka, E. Ressouche, M. R. Lees, and G. Balakrishnan, Evidence for dynamic kagome ice, Nat. Commun. 9, 1 (2018).

25. R. S. W. Braithwaite, K. Mereiter, W. H. Paar, and A. M. Clark, Herbertsmithite, $Cu_3Zn(OH)_6Cl_2$, a new species, and the definition of paratacamite, Mineral. Mag. 68, 527 (2004).

26. K. Zhao, H. Deng, H. Chen, K. A. Ross, V. Petříček, G. Günther, M. Russina, V. Hutanu, and P. Gegenwart, Realization of the kagome spin ice state in a frustrated intermetallic compound, Science 367, 1218 (2020).

27. Z. Wang, H. Zhao, M. Lyu, J. Xiang, Y. Isikawa, S. Zhang, and P. Sun, Frustrated antiferromagnetism and heavy-fermion-like behavior in PrPdAl, Phys. Rev. B 105, 125113 (2020).

28. H. Ge, L. Zhang, N. Zhao, J. Yang, L. Wang, L. Zhou, Y. Fu, T. T. Li, Z. M. Song, F. Ding, J. B. Xu, Y. F. Zhang, S. M. Wang, J. W. Mei, X. Tong, P. Miao, H. He, Q. Zhang, L. S. Wu, and J. M. Sheng, Successive magnetic orderings in the Ising spin chain magnet $DyNi_5Ge_3$, Phys. Rev. Mater. 6, 085001 (2022).

29. B. R. Ortiz, L. C. Gomes, J. R. Morey, M. Winiarski, M. Bordelon, J. S. Mangum, I. W. H. Oswald, J. A. Rodriguez- Rivera, J. R. Neilson, S. D. Wilson, E. Ertekin, T. M. McQueen, and E. S. Toberer, New kagome prototype materials: discovery of KV_3Sb_5, RbV_3Sb_5, and CsV_3Sb_5, Phys. Rev. Mater. 3, 094407 (2019).

30. B. R. Ortiz, P. M. Sarte, E. M. Kenney, M. J. Graf, S. M. L. Teicher, R. Seshadri, and S. D. Wilson, Superconductivity in the Z_2 kagome metal KV_3Sb_5, Phys. Rev. Mater. 5, 034801 (2021).

31. Y. Qiangwei, Z. Tu, C. Gong, Y. Fu, S. Yan, and H. Lei, Superconductivity and normal-state properties of kagome metal RbV_3Sb_5 single crystals, Chin. Phys. Lett. 38, 037403 (2021).

32. B. R. Ortiz, S. M. L. Teicher, Y. Hu, J. L. Zuo, P. M. Sarte, E. C. Schueller, A. M. M. Abeykoon, M. J. Krogstad, S. Rosenkranz, R. Osborn, R. Seshadri, L. Balents, J. He, and S. D. Wilson, CsV3Sb5: A Z_2 topological kagome metal with a superconducting ground state, Phys. Rev. Lett. 125, 247002 (2020).

33. K. Jiang, T. Wu, J. X. Yin, Z. Wang, M. Z. Hasan, S. D. Wilson, X. Chen, and J. Hu, Kagome superconductors AV_3Sb_5 (A= K, Rb, Cs), Nat. Sci. Rev. 10, 199 (2023).

34. T. Neupert, M. M. Denner, J. X. Yin, R. Thomale, and M. Z. Hasan, Charge order and superconductivity in kagome materials, Nat. Phys. 18, 137 (2022).

35. C. Hui, B. Hu, Y. Ye, H. Yang, and H. Gao, Superconductivity and unconventional density waves in vanadium-based kagome materials AV_3Sb_5, Chin. Phys. B 31, 097405 (2022).

36. T. Rina, Y. Yamakawa, S. Onari, and H. Kontani, Mechanism of exotic density-wave and beyond-Migdal unconventional superconductivity in kagome metal AV3Sb5 (A= K, Rb, Cs), Sci. Adv. 8, 4108 (2022).

37. L. Hailan, Q. Gao, H. Liu, Y. Gu, D. Wu, C. Yi, J. Jia, S. Wu, X. Luo, Y. Xu, L. Zhao, Q. Wang, H. Mao, G. Liu, Z. Zhu, Y. Shi, K. Jiang, J. Hu, Z. Xu, and X. J. Zhao, Electronic nature of charge density wave and electron-phonon coupling in kagome superconductor KV_3Sb_5, Nat. Commun. 13, 1 (2022).

38. Y. X. Jiang, X. Y. Yin, M. M. Denner, N. Shumiya, B. R. Ortiz, G. Xu, Z. Guguchia, J. He, M. D. Hossain, X. Liu, J. Ruff, L. Kautzsch, S. S. Zhang, G. Chang, I. Belopolski, Q. Zhang, T. A. Cochran, D. Multer, M. Litskevich, Z. J. Cheng, X. P. Yang, X. P. Wang, Z. Wang, R. Thomale, T. Neupert, S. D. Wilson, and M. Z. Hasan, Unconventional chiral charge order in kagome superconductor KV_3Sb_5, Nat. Mater. 20, 1353 (2021).

39. Y. M. Oey, F. Kaboudvand, B. R. Ortiz, R. Seshadri, and S. D. Wilson, Tuning charge-density wave order and superconductivity in the kagome metals $KV_3Sb_{\{5-x\}}Sn_x$ and $RbV_3Sb_{\{5-x\}}Sn_x$, Phys. Rev. Mater. 6, 074802 (2022).

40. M. Liu, T. Han, X. Hu, Y. Tu, Z. Zhang, M. Long, X. Hou, Q. Mu, and L. Shan, Evolution of superconductivity and charge density wave through Ta and Mo doping in CsV_3Sb_5, Phys. Rev. B 106, 140501 (2022).

41. Y. Li, Q. Li, X. Fan, J. Liu, Q. Feng, M. Liu, C. Wang, J. X. Yin, J. Duan, X. Li, Z. Wang, H. H. Wen, and Y. Yao Tuning the competition between superconductivity and charge order in the kagome superconductor $Cs(V_{1-x}Nb_x)_3Sb_5$, Phys. Rev. B 105, 180507 (2022).

42. Y. Liu, Y. Wang, Y. Cai, Z. Hao, X. M. Ma, L. Wang, C. Liu, J. Chen, L. Zhou, J. Wang, S. Wang, H. He, Y. Liu, S. Cui, B. Huang, J. Wang, C. Chen, and J. W. Mei, Doping evolution of superconductivity, charge order and band topology in hole-doped topological kagome superconductors $Cs(V_{\{1-x\}}Ti_x)_3Sb_5$, Phys. Rev. Mater. 7, 064801 (2023)

43. Y. M. Oey, B. R. Ortiz, F. Kaboudvand, J. Frassineti, E. Garcia, R. Cong, S. Sanna, V. F. Mitrović, R. Seshadri, and S. D. Wilson, Fermi level tuning and double-dome superconductivity in the kagome metal $CsV_3Sb_{5-x}Sn_x$, Phys. Rev. Mater. 6, 041801 (2022).

44. D. Werhahn, B. R. Ortiz, A. K. Hay, S. D. Wilson, R. Seshadri, and D. Johrendt, The kagomé metals $RbTi_3Bi_5$ and $CsTi_3Bi_5$, Z. Naturforschung. B 77, 757 (2022).

45. Y. Wang, Y. Liu, Z. Hao, W. Cheng, J. Deng, Y. Wang, Y. Gu,; X. M. Ma, H. Rong, F. Zhang, S. Guo, C. Zhang, Z. Jiang, Y. Yang, W. Liu, Q. Jiang, Z. Liu, M. Ye, D. Shen, Y. Liu, S. Cui, L. Wang, C. Liu, , J. Lin, Y. Liu, Y. Cai, J. Zhu, C. Chen, and J. W. Mei, Flat Band and $\mathbb{Z}_2$ Topology of Kagome Metal CsTi3Bi5, Chin. Phys. Lett. 40, 037102 (2023).

46. H. Yang, Z. Zhao, X. W. Yi, J. Liu, J. Y. You, Y. Zhang, H. Guo, X. Lin, C. Shen, H. Chen, X. Dong, G. Su, H. J. Gao, Titanium-based kagome superconductor $CsTi_3Bi_5$ and topological states, arXiv preprint arXiv:2209.03840 (2022)

47. Y. Hu, C. Le, Y. Zhang, Z. Zhao, J. Liu, J. Ma, N. C. Plumb, M. Radovic, H. Chen, A.P. Schnyder, X. Wu, X. Dong, J. Hu, H. Yang, H. J. Gao, and M. Shi, Non-trivial band topology and orbital-selective electronic nematicity in a new titanium-based kagome superconductor, Nat. Phys., 1 (2023)

48. X. Chen, X. Liu, W. Xia, X. Mi, L. Zhong, K. Yang, L. Zhang, Y. Gan, Y. Liu, G. Wang, A. Wang, Y. Chai, J. Shen, X. Yang, Y. Guo, and M. He, Electrical and thermal transport properties of kagome metals ATi_3Bi_5 (A = Rb, Cs), Phys. Rev. B 107, 174510 (2023).

49. Y. Zhou, L. Chen, X. Ji, C. Liu, K. Liao, Z. Guo, J. O. Wang, H. Weng, and G. Wang, Physical properties, electronic structure, and strain-tuned monolayer of the weak topological insulator $RbTi_3Bi_5$ with Kagome lattice, arXiv preprint arXiv:2301.01633 (2023)

50. Y. Yang, W. Fan, Q. Zhang, Z. Chen, X. Chen, T. Ying, X. Wu, X. Yang, F. Meng, G. Li, S. Li, L. Gu, T. Qian, A. P. Schnyder, J. Guo, and X. Chen, Discovery of two families of VSb-based compounds with V-kagome lattice, Chin. Phys. Lett. 38, 127102 (2021).

51. Y. Yang, R. Wang, M. Z. Shi, Z. Wang, Z. Xiang, and X. H. Chen, Type-II nodal line fermions in the Z_2 topological semimetals AV_6Sb6 (A = K, Rb, and Cs) with a kagome bilayer, Phys. Rev. B 104, 245128 (2021).

52. M. Shi, F. Yu, Y. Yang, F. Meng, B. Lei, Y. Luo, Z. Sun, J. He, R. Wang, Z. Jiang, Z. Liu, D. Shen, T. Wu, Z.; Xiang, Z. Wang, J. Ying, and X. Chen, A new class of bilayer kagome lattice compounds with Dirac nodal lines and pressure-induced superconductivity, Nat. Commun. 13, 1 (2022).

53. Q. Yin, Z. Tu, C. Gong, S. Tian, and H. Lei, Structures and physical properties of v-based kagome metals CsV_6Sb_6 and CsV_8Sb_{12}. Chin. Phys. Lett. 38, 127401 (2021).

54. K. Kovnir, Predictive synthesis, Chem. Mater. 33, 4835 (2021).

55. M. G. Kanatzidis, Discovery-synthesis, design, and prediction of chalcogenide phases, Inorg. Chem. 56, 3158 (2017).

56. D. L. M. Cordova, and D. C. Johnson, Synthesis of Metastable Inorganic Solids with Extended Structures, ChemPhysChem 21, 1345 (2020).

57. X. Ma, F. Xu, T. M. Atkins, A. M. Goforth, D. Neiner, A. Navrotsky, and S. M. Kauzlarich, A versatile low temperature synthetic route to Zintl phase precursors: Na_4Si_4, Na_4Ge_4 and K_4Ge_4 as examples, Dalton Trans. 46, 10250 (2009).

58. J. V. Zaikina, M. Batuk, A. M. Abakumov, A. Navrotsky, and S. M. Kauzlarich, Facile Synthesis of $Ba_{1-x}K_xFe_2As_2$ Superconductors via Hydride Route, J. Am. Chem. Soc. 136, 16932 (2004).

59. V. Gvozdetskyi, M. P. Hanrahan, R. A. Ribeiro, T. H. Kim, L. Zhou, A. J. Rossini, P. C. Canfield, and J. V. Zaikina, A hydride route to ternary alkali metal borides: a case study of lithium nickel borides, Chem. Eur. J. 25, 4123 (2019).

60. V. Gvozdetskyi, G. Bhaskar, M. Batuk, X. Zhao, R. Wang, S. L. Carnahan, M. P. Hanrahan, R. A. Ribeiro, P. C. Canfield, A. J. Rossini, C. Z. Wang, K. M. Ho, J. Hadermann, and J. V. Zaikina, Computationally driven discovery of a family of layered LiNiB polymorphs, Angew. Chem. Int. Ed. 58, 15855 (2019)

61. T. Cox, V. Gvozdetskyi, B. Owens-Baird, and J.V. Zaikina, Rapid Phase Screening via Hydride Route: A Discovery of $K_{8-x}Zn_{18+3x}Sb_{16}$, Chem. Mater. 30, 8707 (2018).

62. A. N. Adeyemi, G. Bhaskar, T. Cox, S. Hong, V. Gvozdetskyi, and J. V. Zaikina, Hydride Precursors in Materials Synthesis, Comprehensive Inorganic Chemistry III, 3rd ed.; Elsevier, 128 (2023)

63. V. Gvozdetskyi, B. Owens-Baird, S. Hong, T. Cox, G. Bhaskar, C. Harmer, Y. Sun, F. Zhang, C. Z. Wang, K. M. Ho, and J. V. Zaikina, From $NaZn_4Sb_3$ to HT-$Na_{1-x}Zn_{4-y}Sb_3$: Panoramic Hydride Synthesis, Structural Diversity, and Thermoelectric Properties, Chem. Mater. 31, 8695 (2019).

64. http://info.eecs.northwestern.edu/FEpredictor

65. B. Meredig, A. Agrawal, S. Kirklin, J. E. Saal, J. W. Doak, A. Thompson, K. Zhang, A. Choudhary, and C. Wolverton, Combinatorial screening for new materials in unconstrained composition space with machine learning, Phys. Rev. B 89, 094104 (2014).

66. D. W. Rudd, D. W. Vose, and S. Johnson, The permeability of niobium to hydrogen, J. Phys. Chem. 66, 351 (1962).

67. R. E. Buxbaum, and A. B. Kinney, Hydrogen transport through tubular membranes of palladium-coated tantalum and niobium, Ind. Eng. Chem. Res. 35, 530 (1996).

68. H. Yukawa, T. Nambu, Y. Matsumoto, N. Watanabe, G. Zhang, and M. Morinaga, Alloy design of Nb-based hydrogen permeable membrane with strong resistance to hydrogen embrittlement. Mater. Trans. 49, 2202 (2008).

69. D.H. Putz, and D.K.B. GbR, Kreuzherrenstr. 102, 53227 Bonn, Germany. Diamond-Crystal and Molecular Structure Visualization.

70. P.J. Chupas, K.W. Chapman, C. Kurtz, J.C. Hanson, P.L. Lee, and C.P. Grey, A versatile sample-environment cell for non-ambient X-ray scattering experiments, J. Appl. Crystallogr. 41, 822 (2008).

71. V. Favre-Nicolin, and R. Černý, FOX, free objects for crystallography: a modular approach to ab initio structure determination from powder diffraction, J. Appl. Crystallogr. 35, 734 (2002).

72. V. Petricek, M. Dusek, and L. Palatinus, JANA: Crystallographic Computing System for Standard and Modulated Structures. (2006)

73. A. L. Spek, Structure validation in chemical crystallography, Acta Crystallogr., Sect. D: Biol. Crystallogr. 65, 148 (2009).

74. See Supplemental Material at [link to be inserted by publisher] for description of the effect of synthesis with varying molar quantities of KH and K on phase purity of KV_6Sb_6; confirmation of preferred orientation observed in the PXRD data for the KV_6Sb_6 phase; Scanning Electron Microscopy data on KV_6Sb_6 pellet obtained via Spark Plasma Sintering; *in-situ* high temperature PXRD and Differential Scanning Calorimetry data that establishes the thermal stability of the KV_6Sb_6 phase; comparison of the experimental high resolution PXRD data for the KV_6Sb_6 phase with monoclinic ($C2/m$) and rhombohedral ($R\overline{3}m$) models and results of Rietveld refinement for the rhombohedral model to validate the crystal structure of KV_6Sb_6; comparison of coordination environment of K, V, Sb in V_3Sb_2, KV_6Sb_6, and KV_3Sb_5; additional magnetic properties data for KV_6Sb_6; details on hydride synthesis of the KV_3Sb_5 phase including PXRD data and magnetic properties for KV_3Sb_5; and Curie-Weiss fit of KV_6Sb_6 susceptibility curve.

75. S. M. Kauzlarich, Chemistry, Structure, and Bonding of Zintl Phases and Ions, *VCH Publishers Inc.: New York, NY, USA,* (1996).

76. T. F. Fässler, Zintl Phases: Principles and Recent Developments. *Book Series: Structure and Bonding*. *Springer: Berlin/Heidelberg, Germany,* 139 (2011).

77. B. Owens-Baird, S. Heinrich, and K. Kovnir, Thermoelectric materials, *Encycl. Inorg. Bioinorg. Chem.*, 1 (2017).

78. H. Zhang, L. Fang, M. B. Tang, Z. Y. Man, H. H. Chen, X. X. Yang, M. Baitinger, Y. Grin, and J. T. Zhao, Thermoelectric properties of $Yb_xEu_{1-x}Cd_2Sb_2$, *J. Chem. Phys.* 133, 194701 (2010).

79. K. Guo, Q. G. Cao, X. J. Feng, M. B. Tang, H. H. Chen, X. Guo, L. Chen, Y. Grin, and J. T. Zhao, Enhanced thermoelectric figure of merit of Zintl phase $YbCd_{2-x}Mn_xSb_2$ by chemical substitution, *Eur. J. Inorg. Chem.* 26, 4043 (2011)

80. J. A. Dolyniuk, B. Owens-Baird, J. Wang, J. V. Zaikina, and K. Kovnir, Clathrate thermoelectrics, *Mater. Sci. Eng. R* 108, 1 (2016).

81. P. Ren, Y. Liu, J. He, T. Lv, J. Gao, and G. Xu, Recent advances in inorganic material thermoelectrics. *Inorg. Chem. Front*. 5, 2380 (2018).

82. A. Bhardwaj, A. Rajput, A. K. Shukla, J. J. Pulikkotil, A. K. Srivastava, A. Dhar, G. Gupta, S. Auluck, D. K. Misra, R. C. Budhani, Mg_3Sb_2-based Zintl compound: a non-toxic, inexpensive and abundant thermoelectric material for power generation, *RSC Adv.* 3, 8504 (2013).

83. E. S. Toberer, A. F. May, B. C. Melot, E. Flage-Larsen, and G. J. Snyder, Electronic structure and transport in thermoelectric compounds AZn_2Sb_2 (A= Sr, Ca, Yb, Eu). *Dalton Trans.* 39, 1046 (2010).

84. F. Gascoin, S. Ottensmann, D. Stark, S. M. Haïle, G. J. Snyder, Zintl phases as thermoelectric materials: tuned transport properties of the compounds $Ca_xYb_{1-x}Zn_2Sb_2$, *Adv. Funct. Mater.* 15, 1860 (2005).